



Naik, S., & Wiggins, S. (2019). Finding normally hyperbolic invariant manifolds in two and three degrees of freedom with Hénon-Heiles-type potential. *Physical Review E*, *100*, [022204].
<https://doi.org/10.1103/PhysRevE.100.022204>

Publisher's PDF, also known as Version of record

License (if available):
CC BY

Link to published version (if available):
[10.1103/PhysRevE.100.022204](https://doi.org/10.1103/PhysRevE.100.022204)

[Link to publication record in Explore Bristol Research](#)
PDF-document


This is the final published version of the article (version of record). It first appeared online via American Physical Society at <https://journals.aps.org/pre/abstract/10.1103/PhysRevE.100.022204> . Please refer to any applicable terms of use of the publisher.

University of Bristol - Explore Bristol Research

General rights

This document is made available in accordance with publisher policies. Please cite only the published version using the reference above. Full terms of use are available:
<http://www.bristol.ac.uk/pure/about/ebr-terms>

Finding normally hyperbolic invariant manifolds in two and three degrees of freedom with Hénon-Heiles-type potential

Shibabrat Naik * and Stephen Wiggins

School of Mathematics, University of Bristol, University Walk, Clifton BS8 1TW, Bristol, United Kingdom



(Received 22 April 2019; published 5 August 2019)

We present a method based on a Lagrangian descriptor for revealing the high-dimensional phase space structures that are of interest in nonlinear Hamiltonian systems with index-1 saddle. These phase space structures include a normally hyperbolic invariant manifold and its stable and unstable manifolds, which act as codimension-1 barriers to phase space transport. In this article, finding the invariant manifolds in high-dimensional phase space will constitute identifying coordinates on these invariant manifolds. The method of Lagrangian descriptor is demonstrated by applying to classical two and three degrees of freedom Hamiltonian systems which have implications for myriad applications in chemistry, engineering, and physics.

DOI: [10.1103/PhysRevE.100.022204](https://doi.org/10.1103/PhysRevE.100.022204)

I. INTRODUCTION

It is now well known that the paradigm of escape from a potential well and the topology of phase space structures that mediate such escape are useful in a broad array of problems such as reaction rates in chemical physics [1–3], ionization of a hydrogen atom under electromagnetic field in atomic physics [4], transport of defects in solid state and semiconductor physics [5], buckling of structures in solid mechanics [6,7], ship dynamics and capsizing [8–10], escape and recapture of comets and asteroids in celestial mechanics [11–13], and escape into inflation or recollapse to singularity in cosmology [14]. Thus a method that can identify the high-dimensional phase space structures can aid established formulas for quantifying the escape rates [15–17]. Since visualization is insufficient for quantifying escape rates and challenging in high-dimensional phase space, we expect the method to diagnose trajectories in the phase space using low-dimensional sections. To this end, in recent literature on chemical reaction dynamics, a trajectory diagnostic method based on low-dimensional sections has been used to detect *reactive islands* which provide insights into calculating reaction rates and sampling rare transition or escape trajectories which are reaction paths in high-dimensional molecular phase space [18–21]. However, benchmarking this method was much needed; and we first applied it to quadratic Hamiltonian systems where the closed-form analytical expression of the invariant manifolds is known [22]. As the next step, in this article, we will focus on nonlinear Hamiltonian systems which have been extensively studied as “built by hand” models of galactic dynamics, ship capsizing, and for demonstrating quantum dynamical tunneling [23–32].

The nonlinear Hamiltonian systems considered here have an underlying Hénon-Heiles type potential with the simplest form of nonlinearity, and show regular, quasiperiodic, and chaotic trajectories along with bifurcations of periodic orbits

[23,29,31,33–35]. A Hénon-Heiles type potential has a well with bottlenecks connecting the region of bounded motion (trapped or interaction region) to unbounded motion, and has rotational symmetry [36,37]. We have adopted them as our first benchmark nonlinear systems because the Hénon-Heiles type potentials have been used to apply new phase space transport methods in chemistry, engineering, and physics [10,26,27,31,34,38–48]. Conservative dynamics on an open potential well has received considerable attention because the phase space structures, normally hyperbolic invariant manifolds (NHIM) and its invariant manifolds [49], explain the intricate fractal structure of escape or transition rates [50–52]. Furthermore, the discrepancies in observed and predicted ionization rates in atomic systems have also been explained by accounting for the topology of these phase space structures. They have also been connected with the breakdown of ergodic assumption that is the basis for using ionization and dissociation rate formulas [53]. This rich literature on chaotic escape of electrons from atoms sets a precedent for applying new methods for finding NHIM and its invariant manifolds in open potential wells [52,54–57]. Thus, in this article, we will verify the trajectory diagnostic method that uses low-dimensional sections to reveal the phase space structures that mediate escape or transition in four or more dimensional phase space.

As we noted earlier, trajectory diagnostic methods which can probe phase space to detect the high-dimensional invariant manifolds have the potential to be applied in multi-degrees-of-freedom models. One such method uses Lagrangian descriptors (LDs) to reveal phase space structures by encoding geometric property of trajectories (such as, phase space arc length, configuration space distance or displacement, and cumulative action or kinetic energy) initialized on a two-dimensional surface [58–61]. The Lagrangian descriptor was originally developed in the context of chaotic transport in time-dependent two-dimensional fluid mechanics. In recent years, it has also been successful in locating a transition state trajectory relevant for calculating chemical reaction paths and rates in molecular phase space [62–64]. Besides, LDs are

*s.naik@bristol.ac.uk

also applicable to both Hamiltonian and non-Hamiltonian systems, arbitrary time dependence such as stochastic and dissipative forcing, and geophysical data from satellite and numerical simulations [61,65–68]. The method of Lagrangian descriptor (LD) is straightforward to implement computationally and it provides a “high resolution” diagnostic of the influence of high-dimensional phase space structure on trajectory behavior. The method of LD encodes the geometry of a trajectory in the initial condition without requiring the spatial derivative of flow map obtained from the time evolved locations of the initial condition. This is achieved by considering a two-dimensional section of the full phase space and discretizing with a dense grid of initial conditions. Even though the trajectories wander off in the phase space, as the initial conditions evolve in time, there is no loss in resolution of the two-dimensional section. Thus, in contrast to inferring the phase space structures from Poincaré sections, LD plots do not suffer from loss of resolution since the effect of the structures are encoded in the initial conditions and there is no need for the trajectory to return to the section. Our objective is to verify this use of Lagrangian descriptors as a diagnostic on two-dimensional sections of high-dimensional phase space structures. This diagnostic is also meant to be used as the preliminary step in computing the normally hyperbolic invariant manifolds (NHIM), its stable, and unstable manifolds using other computational means [20,69,70]. In this article, we will present the method’s capability to detect the high-dimensional phase space structures such as the NHIM, its stable, and unstable manifolds in two and three DOF Hamiltonian systems.

II. MODELS AND METHOD

A. Model system: Coupled harmonic two DOF Hamiltonian

As pointed out in the Introduction, we will focus on a well-understood model system which is a two degrees-of-freedom coupled harmonic oscillator with the Hamiltonian

$$\begin{aligned} \mathcal{H}(x, y, p_x, p_y) &= T(p_x, p_y) + V_B(x, y) \\ &= \frac{1}{2}p_x^2 + \frac{1}{2}p_y^2 + \frac{1}{2}\omega_x^2x^2 + \frac{1}{2}\omega_y^2y^2 + \delta xy^2, \end{aligned} \quad (1)$$

where $\omega_x, \omega_y, \delta$ are the harmonic oscillation frequencies of the x, y degree of freedom and the coupling strength, respectively. We will fix the parameters as $\omega_x = 1.0$, $\omega_y = 1.1$, and $\delta = -0.11$ in this study. This two degrees-of-freedom potential is also referred to as *Barbanis* potential, and has been investigated as a model of galactic motion [23,33], dynamical tunneling and molecular spectra in physical chemistry [26,71,72], and structural mechanics and ship capsizes [9,10].

The equilibria of the Hamiltonian vector field are located at

$$\left(-\frac{\omega_y^2}{2\delta}, \pm \frac{1}{\sqrt{2}} \frac{\omega_x\omega_y}{\delta}, 0, 0 \right), \quad (0, 0, 0, 0) \quad (2)$$

and are at total energy $E_c = \frac{\omega_x^2\omega_y^4}{8\delta^2}$ and zero, respectively. The two index-1 saddle equilibria (defined and shown in Appendix A 1 a) are located at positive and negative y coordinate with positive x coordinate for $\delta < 0$. The total energy of the two

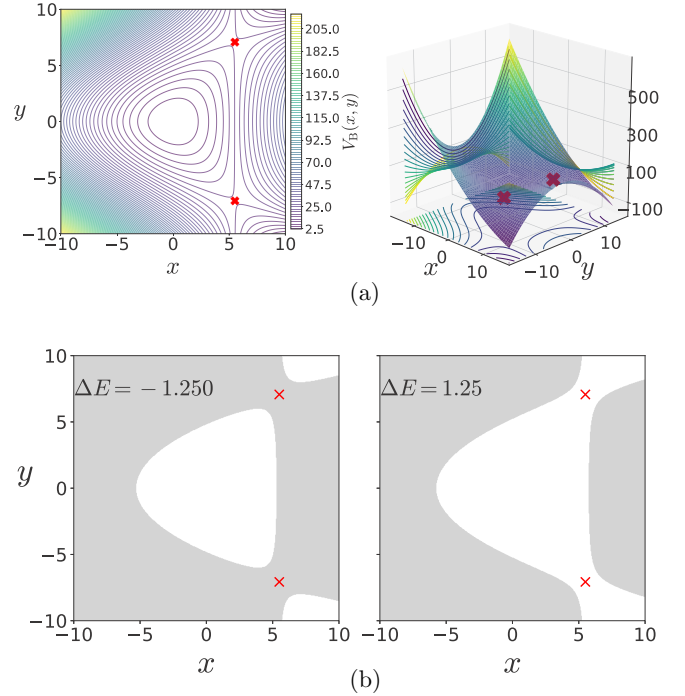


FIG. 1. (a) Potential energy function underlying the coupled harmonic Hamiltonian (1) as isopotential contour and surface. The index-1 saddles are shown as red crosses in both the plots. (b) Hill’s region for energy below and above the total energy of the index-1 saddle equilibria. The gray region denotes energetically inaccessible configuration space projection and unbounded motion or escape from the potential well is only possible for positive excess energy, ΔE . Here, the parameters in Eq. (1) are $\omega_x = 1.0$, $\omega_y = 1.1$, $\delta = -0.11$.

index-1 saddle equilibria will be referred to as *critical energy*, E_c . In our discussion, we will refer to the total energy of a trajectory or initial condition in terms of the excess energy, $\Delta E = E_c - e$, which can be negative or positive to denote energy below or above the critical energy. For the parameters used in this study, the index-1 saddle equilibria are at $(5.5, \pm 7.071, 0, 0)$ and have total energy, $E_c = 15.125$.

The contours of the coupled harmonic two DOF potential energy function in Eq. (1) is shown in Fig. 1(a) along with the 3D view of the surface. We note here that the potential has steep walls for $x < 0$ when $\delta < 0$ and steep dropoff beyond the bottlenecks around the index-1 saddles. This leads to unphysical motion in the sense of trajectories approaching $-\infty$ with ever increasing acceleration even for finite values of the configuration space coordinates [24].

In Fig. 1(b) we show the *Hill’s region*, as defined in Appendix A, for the model system (1). It is important to note here that even though Hill’s region is shown on the configuration space, it captures the dynamical picture, that is the *phase space perspective*, of the Hamiltonian. This visualization of the energetically accessible and forbidden realm is the first step towards introducing two-dimensional surfaces that diagnose trajectory behavior. The complete description of the unstable periodic orbit and its invariant manifolds is described in Appendix A 2 along with the visualization in the 3D space.

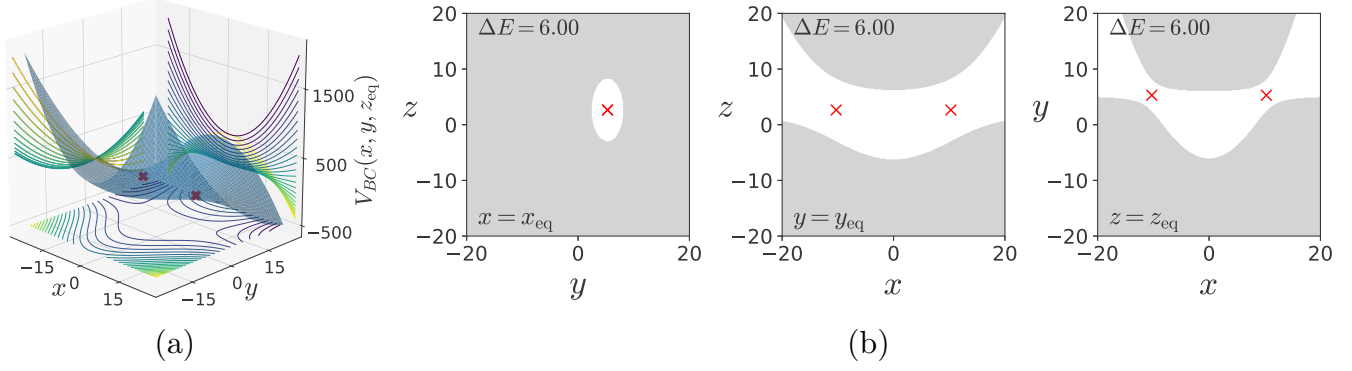


FIG. 2. (a) Potential energy function underlying the coupled harmonic Hamiltonian (4) at $z_{\text{eq}} = 2.647$ as isopotential contour and surface. (b) Hill's region for excess energy, $\Delta E = 6.000$, projected on the configuration space at the rank-1 saddle equilibrium point $(x_{\text{eq}}, y_{\text{eq}}, z_{\text{eq}}, 0, 0, 0)$. We note here that the potential energy surface and the Hill's region is plotted by fixing one of the configuration coordinates at the equilibrium point.

Since this model system is conservative two DOF Hamiltonian, that is, the phase space is \mathbb{R}^4 , the energy surface is three dimensional, the dividing surface is two dimensional, and the normally hyperbolic invariant manifold (NHIM), referred to as the unstable periodic orbit, is one dimensional [73]. Now, if we consider the intersection of a two-dimensional surface with the three-dimensional energy surface, we would obtain the one-dimensional energy boundary on the surface of section. We will focus our study by using the isoenergetic two-dimensional surface

$$U_{xp_x}^+ = \{(x, y, p_x, p_y) \mid y = 0, p_y(x, y, p_x; e) > 0\}, \quad (3)$$

where the sign of the momentum coordinate enforces a directional crossing of the surface. Due to the form of the vector field (A1) and choice of $\delta < 0$, this directionality condition implies motion towards positive y coordinate.

In this article, detecting the phase space structures will constitute finding the intersection of the NHIM and its invariant manifolds with a two-dimensional surface [for example, Eq. (3)].

B. Model system: Coupled harmonic three DOF Hamiltonian

The next higher-dimensional model system to consider is the coupled harmonic potential in three dimensions and underlying a three degrees-of-freedom system in [34,74]. The Hamiltonian is given by

$$\begin{aligned} \mathcal{H}(x, y, z, p_x, p_y, p_z) &= T(p_x, p_y, p_z) + V_{\text{BC}}(x, y, z) \\ &= \frac{1}{2}p_x^2 + \frac{1}{2}p_y^2 + \frac{1}{2}p_z^2 + \frac{1}{2}\omega_x^2 x^2 + \frac{1}{2}\omega_y^2 y^2 + \frac{1}{2}\omega_z^2 z^2 \\ &\quad - \epsilon x^2 y - \eta x^2 z, \end{aligned} \quad (4)$$

where $\omega_x^2, \omega_y^2, \omega_z^2, \epsilon, \eta$ are the parameters related to the coupled harmonic three-dimensional potential energy function [74]. In this study, we will fix the parameters to be $\omega_x^2 = 0.9$, $\omega_y^2 = 1.6$, $\omega_z^2 = 0.4$, $\epsilon = 0.08$, and $\eta = 0.01$. The two index-1 saddle equilibria (as shown in Appendix B) of the

Hamiltonian vector field (B1) are

$$\begin{aligned} &(x_{\text{eq}}, y_{\text{eq}}, z_{\text{eq}}, 0, 0, 0) \\ &= \left(\pm \frac{\omega_x \omega_y \omega_z}{\sqrt{2(\epsilon^2 \omega_z^2 + \eta^2 \omega_y^2)}}, \frac{\epsilon \omega_x^2 \omega_z^2}{2(\epsilon^2 \omega_z^2 + \eta^2 \omega_y^2)}, \right. \\ &\quad \left. \times \frac{\eta \omega_x^2 \omega_y^2}{2(\epsilon^2 \omega_z^2 + \eta^2 \omega_y^2)}, 0, 0, 0 \right) \end{aligned} \quad (5)$$

and the total energy is

$$E_c = \frac{1}{8} \omega_x^2 \frac{\omega_x^2 \omega_y^2 \omega_z^2}{(\epsilon^2 \omega_z^2 + \eta^2 \omega_y^2)}. \quad (6)$$

The equilibrium point at $(0,0,0,0,0,0)$ is stable and has total energy zero. For the parameters used in this study, the equilibria are located at $(\pm 10.290, 5.294, 2.647, 0, 0, 0)$ and $(0, 0, 0, 0, 0, 0)$ and have total energy $E_c \approx 23.824$ and $E = 0$, respectively. We show the isopotential contours of the potential energy function at fixed value of z_{eq} in Fig. 2 along with the Hill's regions for positive excess energy, $\Delta E = 6.000$, and projected on the configuration space coordinates at the equilibrium point.

Since this model system is conservative three DOF Hamiltonian, that is the phase space is \mathbb{R}^6 , the energy surface is five dimensional, the dividing surface is four dimensional, and the normally hyperbolic invariant manifold (NHIM) is three dimensional, or precisely three-sphere, and its invariant manifolds are four dimensional, or precisely $\mathbb{R}^1 \times \mathbb{S}^3$ or *spherical cylinders* [73]. Now, if we consider the intersection of a two-dimensional section with the five-dimensional energy surface in \mathbb{R}^6 , we would obtain the one-dimensional energy boundary on the surface. We will focus our study near the bottleneck by considering the isoenergetic two-dimensional surfaces:

$$U_{xp_x}^+ = \{(x, y, z, p_x, p_y, p_z) \mid y = y_{\text{eq}}, z = z_{\text{eq}}, p_y = 0, p_z(x, y, z, p_x, p_y; e) > 0\}, \quad (7)$$

$$U_{yp_y}^+ = \{(x, y, z, p_x, p_y, p_z) \mid x = x_{\text{eq}}, z = z_{\text{eq}}, p_x = 0, p_z(x, y, z, p_x, p_y; e) > 0\}, \quad (8)$$

$$U_{zp_z}^+ = \{(x, y, z, p_x, p_y, p_z) \mid x = x_{\text{eq}}, y = y_{\text{eq}}, p_x = 0, p_y(x, y, z, p_x, p_z; e) > 0\}. \quad (9)$$

In this three DOF system, detecting points on the three-dimensional NHIM and four-dimensional invariant manifolds will constitute finding their intersection with the above two-dimensional surfaces.

C. Method: Lagrangian descriptor

The Lagrangian descriptor (LD) as presented in Ref. [58] is the arc length of a trajectory calculated on a chosen initial time t_0 and measured for fixed forward and backward integration time, τ . For continuous time dynamical systems, Ref. [61] gives an alternative definition of the LD which is useful for proving rigorous results and can be computed along with the trajectory. It provides a characterization of the notion of singular features of the LD that facilitates a proof for detecting invariant manifolds in certain model situations. In addition, the ‘‘additive nature’’ of this new definition of LD provides an approach for assessing the influence of each degree of freedom separately. This property was used in Ref. [75] to show that Lagrangian descriptor can detect Lyapunov periodic orbits in the two degrees-of-freedom Hénon-Heiles system. We will adopt a similar strategy for the aforementioned two and three degrees-of-freedom autonomous Hénon-Heiles type systems.

In the general setting of a time-dependent vector field

$$\frac{d\mathbf{x}}{dt} = \mathbf{v}(\mathbf{x}, t), \quad \mathbf{x} \in \mathbb{R}^n, \quad t \in \mathbb{R}, \quad (10)$$

where $\mathbf{v}(\mathbf{x}, t) \in C^r$ ($r \geq 1$) in \mathbf{x} and continuous in time. The definition of LDs depends on the initial condition $\mathbf{x}_0 = \mathbf{x}(t_0)$, on the initial time t_0 (trivial for autonomous systems) and the integration time τ , and the type of norm of the trajectory’s components, and takes the form

$$M_p(\mathbf{x}_0, t_0, \tau) = \int_{t_0-\tau}^{t_0+\tau} \sum_{i=1}^n |\dot{x}_i(t; \mathbf{x}_0)|^p dt, \quad (11)$$

where $p \in (0, 1]$ and $\tau \in \mathbb{R}^+$ are freely chosen parameters and the overdot symbol represents the derivative with respect to time. It is to be noted here that there are three formulations of the function M_p in the literature: the arc length of a trajectory in phase space [58], the arc length of a trajectory projected on the configuration space [19,20,76,77], and the sum of the p norm of the vector field components [61,78]. Although the latter formulation of the Lagrangian descriptor (11) developed in Refs. [61,78] does not resemble the arc length, the numerical results using either of these forms have been shown to be in agreement and promise of predictive capability in geophysical flows [65–68]. The form of LD adopted here is motivated by the fact that this allows for proving rigorous results, which we will discuss in the next section, connecting the singular features and minimum in the LD plots with NHIM and its stable and unstable manifolds. It follows from the result that

$$\mathcal{W}^s(\mathbf{x}_0, t_0) = \operatorname{argmin} \mathcal{L}^{(f)}(\mathbf{x}_0, t_0, \tau), \quad (12)$$

$$\mathcal{W}^u(\mathbf{x}_0, t_0) = \operatorname{argmin} \mathcal{L}^{(b)}(\mathbf{x}_0, t_0, \tau), \quad (13)$$

where the stable and unstable manifolds $[\mathcal{W}^s(\mathbf{x}_0, t_0)$ and $\mathcal{W}^u(\mathbf{x}_0, t_0)]$ denote the invariant manifolds at initial time t_0

and $\operatorname{argmin}(\cdot)$ denotes the argument that minimizes the function $\mathcal{L}^{(\cdot)}(\mathbf{x}_0, t_0, \tau)$ in forward and backward time, respectively. In addition, the coordinates on the NHIM, $\mathcal{M}(\mathbf{x}_0, t_0)$, at time t_0 is given by the intersection $\mathcal{W}^s(\mathbf{x}_0, t_0)$ and $\mathcal{W}^u(\mathbf{x}_0, t_0)$ of the stable and unstable manifolds, and thus given by

$$\begin{aligned} \mathcal{M}(\mathbf{x}_0, t_0) &= \operatorname{argmin} (\mathcal{L}^{(f)}(\mathbf{x}_0, t_0, \tau) + \mathcal{L}^{(b)}(\mathbf{x}_0, t_0, \tau)) \\ &= \operatorname{argmin} \mathcal{L}(\mathbf{x}_0, t_0, \tau). \end{aligned} \quad (14)$$

In applying the LD method to nonlinear systems, one observes multiple minima and singularities that can lead to trouble with isolating the one minimum corresponding to the NHIM and the ones due to its invariant manifolds. Since, as we integrate initial conditions on an isoenergetic two-dimensional surface such as $U_{xp_x}^+$ (3), almost all trajectories that escape to infinity get integrated for the entire time interval and result in numerical overflow of the function M value (11) and show up as NaN. This can, however, be avoided by integrating for shorter time interval but this will vary for different locations of a surface, thus leading to trouble in locating the point with minimum and singularity in the LD contour map that corresponds to NHIM and its invariant manifolds.

This computational issue has been addressed in recent efforts to locate transition state trajectory in driven and three degrees-of-freedom chemical reaction dynamics [63,79,80]. It has been noted that computing a fixed integration time Lagrangian descriptor (LD) as given by Eq. (11) leads to two potential issues.

(1) Bounded trajectories will show global recrossings of the barrier as predicted by the Poincaré recurrence theorem. The recrossings will show multiple minima and singularities [as in Figs. 3(d)–3(f)] in the LD plot which obscures locating the actual NHIM.

(2) The trajectories that escape the potential well will leave with ever increasing acceleration, if the potential energy surface opens out to infinity. The trajectories with NaN LD values will render the contour map flat which again obscures locating the NHIM.

To circumvent these issues, a heuristic that has been adopted in the chemical reaction dynamics literature is to calculate LD values only until a trajectory remains inside the barrier region [19,69,81]. The immediate result is the initial condition on an invariant manifold will give a maxima in the LD contour map because of being integrated for the full integration time (preselected) interval.

Thus the form (11) is modified as

$$M_p(\mathbf{x}_0, t_0, \tau^\pm) = \int_{t_0-\tau^-}^{t_0+\tau^+} \sum_{i=1}^n |\dot{x}_i(t; \mathbf{x}_0)|^p dt, \quad (15)$$

where the integration time interval depends on a trajectory and given by

$$\tau^\pm(\mathbf{x}_0) = \min(\tau, t|_{|\mathbf{x}(t)| > q_s}), \quad (16)$$

where q_s defines a domain, called the *saddle region*, in the configuration space around the saddle in the bottleneck. We note here that the only initial condition that gets integrated for the entire τ time units in forward and backward time is the one on the NHIM. In addition, the coordinates on the NHIM,

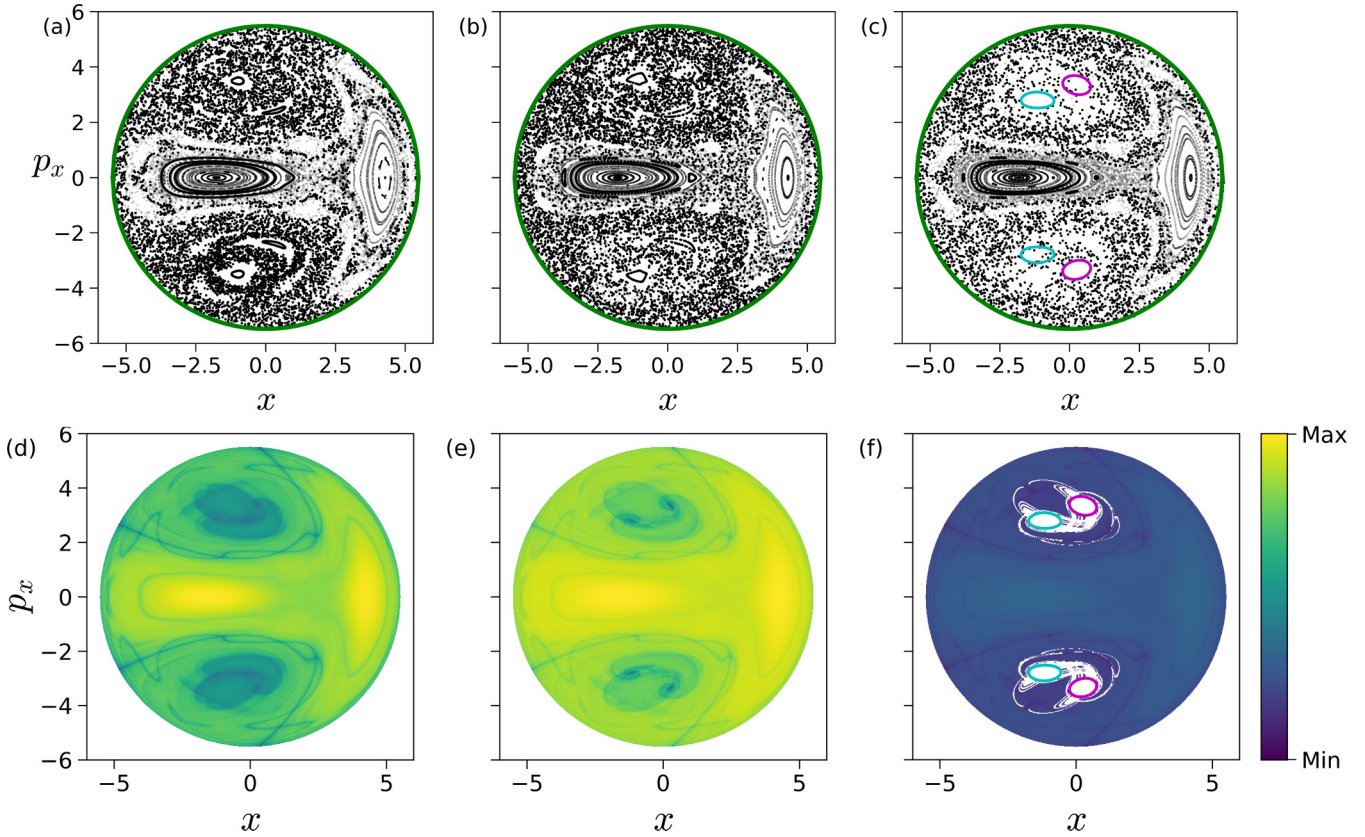


FIG. 3. *Top row:* Poincaré surface of section, $U_{xp_x}^+$ (3), at excess energy (a) $\Delta E = -0.125$, (b) $\Delta E = 0.000$, and (c) $\Delta E = 0.125$, where the intersection of the surface of section with the energy surface is shown in green. *Bottom row:* Lagrangian descriptor on the surface of section, $U_{xp_x}^+$ (3), for the excess energies (d) $\Delta E = -0.125$, (e) $\Delta E = 0.000$, and (f) $\Delta E = 0.125$ and the integration time $\tau = 50$. The intersection of the surface of section with the cylindrical manifolds of the NHIM—unstable periodic orbit for this system—associated with the index-1 saddle equilibrium point in the bottleneck is shown in cyan (stable) and magenta (unstable) curves. The magenta and cyan curves in $p_x > 0$ correspond to the invariant manifolds of unstable periodic orbit at $y > 0$ index-1 saddle and the ones in $p_x < 0$ correspond to the invariant manifolds of unstable periodic orbit at $y < 0$ index-1 saddle.

$\mathcal{M}(\mathbf{x}_0, t_0)$, at time t_0 are given by

$$\begin{aligned} \mathcal{M}(\mathbf{x}_0, t_0) &= \operatorname{argmax} (\mathcal{L}^{(f)}(\mathbf{x}_0, t_0, \tau) + \mathcal{L}^{(b)}(\mathbf{x}_0, t_0, \tau)) \\ &= \operatorname{argmax} \mathcal{L}(\mathbf{x}_0, t_0, \tau). \end{aligned} \tag{17}$$

The variable integration time Lagrangian descriptor as given by Eq. (15) to locate invariant manifolds is familiar in the dynamical systems community. It is related to computing average exit times to locate invariant sets in the phase space of symplectic maps [82]. However, the connection between features in exit times and variable integration time LD contour maps is not the focus of this study and will be deferred as related future work.

III. RESULTS AND DISCUSSIONS

We begin by noting that two-dimensional Poincaré surface of section have sufficient dimensionality to capture trajectories on a three-dimensional energy surface; however, for high-dimensional systems trajectories can go “around” the two-dimensional surface. One approach available in the literature is to use high-dimensional Poincaré sections which can “catch” trajectories but are hard to visualize on paper or in the virtual 3D space. Even when one gets around this

issue, using suitable projective geometry, the fact that the qualitative analysis based on Poincaré sections depends on trajectories returning to this surface cannot be circumvented since trajectories on and inside the spherical cylinders will not return to the Poincaré surface of section.

A. Coupled harmonic two DOF system

As discussed in aforementioned literature [58,61,75], points with minimum Lagrangian descriptor (LD) values and singularity are on the invariant manifolds. In addition, LD plots show dynamical correspondence with Poincaré sections (in the sense that regions with regular and chaotic dynamics are distinct in both the Poincaré section and LD plots), while also depicting the geometry of manifold intersections [61,75,83]. This correspondence in the LD features and Poincaré section is confirmed in Fig. 3, where we show the Poincaré surface of section Eq. (3) of trajectories and LD contour maps on the same isoenergetic two-dimensional surface for negative and positive excess energies. It can be seen that the chaotic dynamics as marked by the sea of points in the Poincaré section is revealed as the tangle of invariant manifolds which are points of minima and singularity in the LD plots. As shown by the one-dimensional slices of the LD

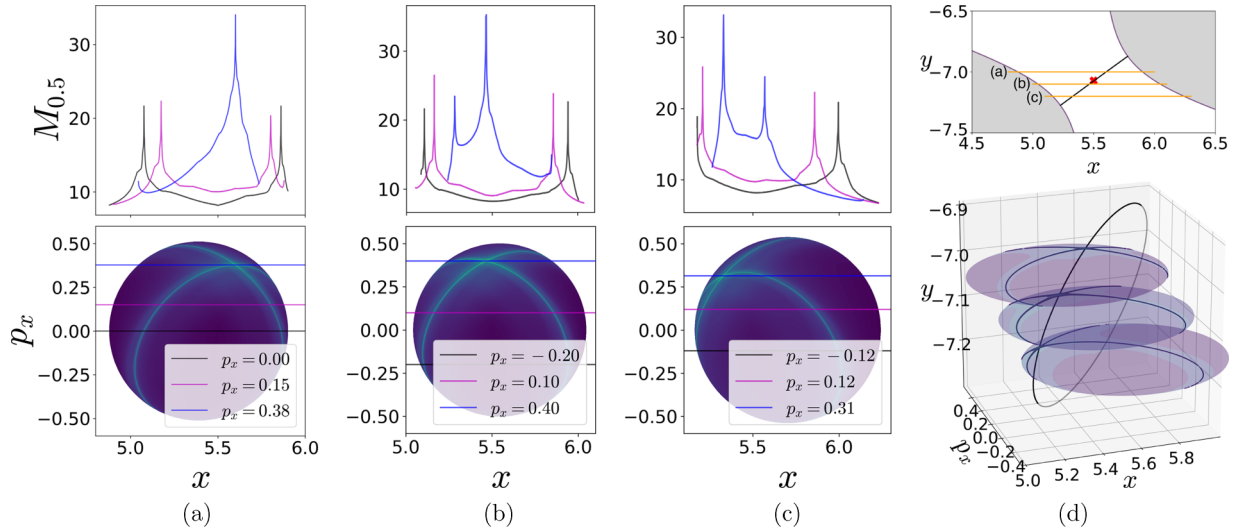


FIG. 4. (a)–(c) Lagrangian descriptor computed for variable integration time on two-dimensional slices (18) near the bottleneck that detect the NHIM and its invariant manifolds associated with the index-1 saddle. (d) The two-dimensional surfaces (a) $U_{xp_x}^+(-7.0)$, (b) $U_{xp_x}^+(-7.1)$, and (c) $U_{xp_x}^+(-7.2)$ as projected on the configuration space (in the top figure as orange lines) and the unstable periodic orbit as black line connecting the isopotential contour corresponding to $\Delta E = 0.125$ with the Hill’s region shown in gray. The two-dimensional slices represent low-dimensional probe of the unstable periodic orbit and the movie of a rotating view can be found here.

plots, there are multiple such minima and singularities and, as the excess energy is increased to positive values, there are regions of discontinuities along the one-dimensional slice. Next, as the energy is increased and the bottleneck opens at critical energy E_c , trajectories that leave the potential well and do not return to the surface of section are not observed on the Poincaré section, while the LD contour maps clearly identify these regions as discontinuities in the LD values. These regions lead to escape because they are inside the cylindrical manifolds of the unstable periodic orbit associated with the index-1 saddle equilibrium point [10]. These regions on the isoenergetic two-dimensional surface are also referred to as *reactive islands* in chemical reaction dynamics [84–86]. The escape regions or reactive islands that appear over the integration time interval can also be identified by using the forward and backward LD contour maps where these regions appear as discontinuities. In Fig. 3(f), we show these for $\Delta E = 0.125$ and $\tau = 50$ along with the intersection of the cylindrical manifolds’ intersections that are computed using differential correction and numerical continuation. The detailed comparison and extension to high-dimensional systems is not the focus of this study and will be discussed in forthcoming work. Thus LD maps also provide a quick and reliable approach for detecting regions that will lead to escape within the observed time, or in the computational context, the integration time.

To detect the NHIM—in this case, unstable periodic orbit—associated with the index-1 saddles [marked by cross in Fig. 1(a)], we define an isoenergetic two-dimensional surface that is parametrized by the y coordinate and placed near the x coordinate of the saddle equilibrium that has the negative y coordinate. This can be expressed as a parametric two-dimensional surface

$$U_{xp_x}^+(k) = \{(x, y, p_x, p_y) | y = k, p_y(x, y, p_x; e) > 0\} \quad (18)$$

for total energy, e , which is above the critical energy, E_c , and k is the y coordinate. The variable integration time LD contour maps are shown in Fig. 4 along with the projection of the low-dimensional slices (18) in the configuration space and the NHIM. The points on NHIM, which is an unstable periodic orbit for two DOF, on this surface is the coordinate with maximum (for variable integration time) LD value. The full visualization of the NHIM as the black ellipse, \mathbb{S}^1 , is in Fig. 4(d) and has been computed using differential correction and numerical continuation (details in Appendix A 2) and shows clearly that points on this unstable periodic orbit are detected by the LD contour map.

B. Coupled harmonic three DOF system

The Lagrangian descriptor based approach for detecting NHIM in the two DOF system can now be applied to the three DOF system (4). On the five-dimensional energy surface, the phase space structures such as the NHIM and its invariant manifolds are three and four dimensional, respectively [73]. As noted earlier, direct visualization techniques will fall short in four or more DOF systems even if they are successful in two and three DOF. So, a LD based approach can be used to detect points on a NHIM and its invariant manifolds using low-dimensional probe which are based on a trajectory diagnostic on an isoenergetic two-dimensional surface.

It is to be noted that the increase in phase space dimension leads to a polynomial scaling in the number of coordinate pairs [that is, $2N(2N - 1)(N - 1)$ coordinate pairs for N DOF system] and is thus impractical to present the procedure on all the combinations of coordinates. We will present the results for the three configuration space coordinates by combining each with its corresponding momentum coordinate.

On these isoenergetic surfaces, we compute the variable integration time Lagrangian descriptor for small excess energy, $\Delta E \approx 0.176$, or total energy $E = 24.000$, and show the

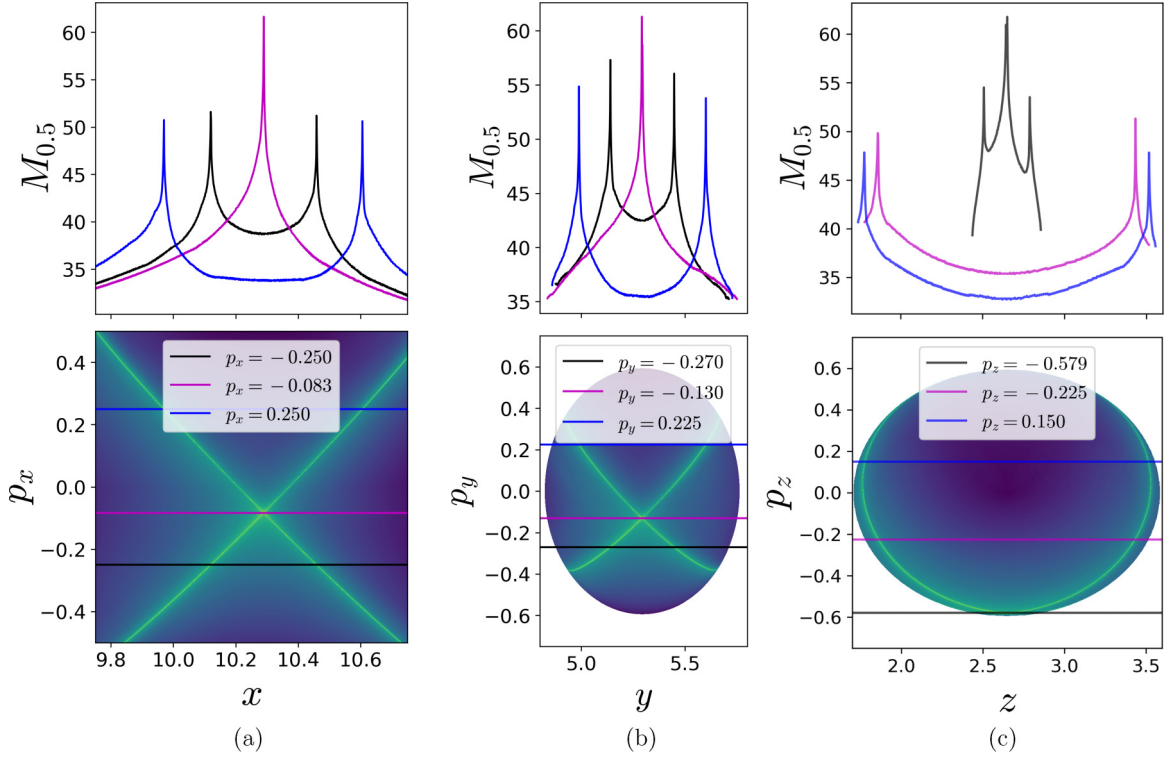


FIG. 5. Detecting coordinates on the NHIM and its invariant manifolds using variable integration time Lagrangian descriptor on the two-dimensional surfaces (a) $U_{xp_x}^+$, (b) $U_{yp_y}^+$, and (c) $U_{zp_z}^+$ defined in Eqs. (7)–(9), respectively, and at excess energy $\Delta E \approx 0.176$ or total energy $E = 24.000$. For this excess energy, the saddle region, as defined in Eq. (16), is taken to be $q_s = [9, 12] \times [2.5, 7.5] \times [1, 4]$ and the preselected integration time $\tau = 50$. The coordinates on the invariant manifolds show up as maxima in the LD contour map and are shown using one-dimensional slices at constant momenta.

contour maps in Fig. 5. The maxima identifying the points on the NHIM and its invariant manifolds can be visualized using one-dimensional slices at constant momenta. This indicates clearly the initial conditions in the phase space [points on the isoenergetic two-dimensional surfaces in \mathbb{R}^6 , for example, Eq. (7)] that do not leave the saddle region.

IV. SUMMARY AND OUTLOOK

In this article, we presented a trajectory diagnostic method as a low-dimensional probe of high-dimensional invariant manifolds in two and three DOF nonlinear Hamiltonian systems with escape or transition dynamics which is ubiquitous in engineering and physical sciences. This trajectory diagnostic method—Lagrangian descriptor (LD)—represents a geometric property of trajectories and is used to reveal the phase space structures without loss of resolution. In addition, features in the LD contour map, that is minima or maxima, identify points on the high-dimensional invariant manifolds that mediate escape or transition dynamics.

Comparing the points on the NHIM in a two DOF system obtained using the LD method with differential correction and numerical continuation, we verified the results for a nonlinear autonomous system following our previous work on decoupled and coupled two and three DOF linear systems [22]. The results on a three DOF system are also congruent with what one expects for an extended problem of the two DOF coupled harmonic potential. Furthermore, the LD method based

detection of NHIM is simple to implement and quickly provides a lay of the dynamical land which is a preliminary step in applying phase space transport. This method can also be used to set up a starting guess for other numerical procedures which rely on a good initial guess or can also be used in conjunction with machine learning methods for rendering smooth pieces of the NHIM and its invariant manifolds [69,81].

ACKNOWLEDGMENTS

We acknowledge the support of EPSRC Grant No. EP/P021123/1 and ONR Grant No. N00014-01-1-0769. We would like to thank Dmitry Zhdanov for stimulating discussions. S.N. would like to thank Shane Ross for introducing him to the Barbanis potential for studying nonlinear dynamics of ship capsizes.

APPENDIX A: COUPLED HARMONIC TWO DOF SYSTEM

For the system (1), Hamilton's equations of motion are

$$\begin{aligned} \dot{x} &= p_x, \\ \dot{y} &= p_y, \\ \dot{p}_x &= -\frac{\partial V}{\partial x} = -(\omega_x^2 x + \delta y^2), \\ \dot{p}_y &= -\frac{\partial V}{\partial y} = -(\omega_y^2 y + 2\delta xy). \end{aligned} \quad (\text{A1})$$

Hill's region and zero velocity curve. The projection of energy surface into configuration space, (x, y) plane, is the region of energetically possible motion for an energy $E(x, y, p_x, p_y) = e$. Let $M(e)$ denote this projection defined as

$$M(e) = \{(x, y) | V_B(x, y) \leq e\}, \quad (\text{A2})$$

where $V_B(x, y)$ is the potential energy function (1). The projection (A2) of energy surface is known in Hamiltonian mechanics as the *Hill's region*. The boundary of $M(e)$ is known as the *zero velocity curve* and plays an important role in placing bounds on a trajectory at a fixed total energy. The zero velocity curve is the locus of points in the (x, y) plane where the kinetic energy and hence the angular velocity vanishes, that is,

$$E(x, y, p_x, p_y) = e = \frac{1}{2}(p_x^2 + p_y^2) + V_B(x, y), \quad (\text{A3})$$

$$p_x^2 + p_y^2 = 2[e - V_B(x, y)] = 0. \quad (\text{A4})$$

From Eq. (A2), it is clear that the state is only able to move on the side of this curve for which the kinetic energy is positive. The other side of the curve, where the kinetic energy is negative and motion is impossible, is referred to as the energetically forbidden realm, and shown as gray region.

Symmetries of the equations of motion. We note the symmetries in the system (A1) by substituting $(-y, -p_y)$ for (y, p_y) , which implies reflection about the x axis and is expressed as

$$s_y : (x, y, p_x, p_y, t) \rightarrow (x, -y, p_x, -p_y, t). \quad (\text{A5})$$

Thus, if $[x(t), y(t), p_x(t), p_y(t)]$ is a solution to (A1), then $[x(t), -y(t), p_x(t), -p_y(t)]$ is another solution. The conservative system also has time-reversal symmetry

$$s_t : (x, y, p_x, p_y, t) \rightarrow (x, y, -p_x, -p_y, -t). \quad (\text{A6})$$

So, if $[x(t), y(t), p_x(t), p_y(t)]$ is a solution to (A1), then $[x(-t), y(-t), -p_x(-t), -p_y(-t)]$ is another solution. These symmetries can be used to decrease the number of computations, and to find special solutions. For example, any solution of (A1) will evolve on the energy surface given by (1). For fixed energy, $E(x, y, p_x, p_y) = e$, there will be zero velocity curves corresponding to $V_B(x, y) = e$, the contours shown in Fig. 1(a). Any trajectory which touches the zero velocity curve at time t_0 must retrace its path in configuration space [i.e., $q = (x, y)$ space],

$$q(-t + t_0) = q(t + t_0), \quad \dot{q}(-t + t_0) = -\dot{q}(t + t_0). \quad (\text{A7})$$

1. Linearized Hamiltonian system

To find the linearized equations around the saddle equilibria with coordinates $(x_e, y_e, 0, 0)$, we need the quadratic terms of the Hamiltonian (1) expanded about the equilibrium point. After making a coordinate change with $(x_e, y_e, 0, 0)$ as the origin, the quadratic terms of the Hamiltonian function for the linearized equations, which we shall call H_l , are given by

$$H_l = \frac{1}{2}p_x^2 + \frac{1}{2}p_y^2 + \frac{1}{2}\omega_x^2 x^2 + \frac{1}{2}\omega_y^2 y^2 + 2\delta xy y_e + \delta y^2 x_e. \quad (\text{A8})$$

This gives the linear equations of motion near the equilibrium point as

$$\begin{pmatrix} \dot{x} \\ \dot{y} \\ \dot{p}_x \\ \dot{p}_y \end{pmatrix} = \begin{pmatrix} 0 & 0 & 1 & 0 \\ 0 & 0 & 0 & 1 \\ -\omega_x^2 & -2\delta y_e & 0 & 0 \\ -2\delta y_e & -(\omega_y^2 + 2\delta x_e) & 0 & 0 \end{pmatrix} \begin{pmatrix} x \\ y \\ p_x \\ p_y \end{pmatrix}. \quad (\text{A9})$$

a. Linear analysis near the equilibria

Studying the linearization of the dynamics near the equilibria is an essential ingredient for understanding the more full nonlinear dynamics. We analyze the linearized dynamics near the saddle equilibrium points which extends to the full nonlinear system due to the generalization of Liapounov's theorem. Here we perform linearization of the vector field (A1) to study the dynamics near the equilibrium points. This is given by the Jacobian, $Df(\mathbf{x})$, of the vector field

$$\mathbb{J} = Df(\mathbf{x}) = \begin{pmatrix} 0 & 0 & 1 & 0 \\ 0 & 0 & 0 & 1 \\ -\omega_x^2 & -2\delta y_e & 0 & 0 \\ -2\delta y_e & -(\omega_y^2 + 2\delta x_e) & 0 & 0 \end{pmatrix}, \quad (\text{A10})$$

where $\mathbf{x} = (x, y, p_x, p_y)$ and $(x_e, y_e, 0, 0)$ is the equilibrium point.

Saddle-center equilibrium. At the equilibria,

$$\left(-\frac{\omega_y^2}{2\delta}, \pm \frac{1}{\sqrt{2}} \frac{\omega_x \omega_y}{\delta}, 0, 0 \right), \quad (\text{A11})$$

the Jacobian (A10) becomes

$$\begin{aligned} \mathbb{J} &= Df(\mathbf{x})|_{(-\frac{\omega_y^2}{2\delta}, \pm \frac{1}{\sqrt{2}} \frac{\omega_x \omega_y}{\delta}, 0, 0)} \\ &= \begin{pmatrix} 0 & 0 & 1 & 0 \\ 0 & 0 & 0 & 1 \\ -\omega_x^2 & \mp \sqrt{2} \omega_x \omega_y & 0 & 0 \\ \mp \sqrt{2} \omega_x \omega_y & 0 & 0 & 0 \end{pmatrix}. \end{aligned} \quad (\text{A12})$$

The characteristic polynomial of the Jacobian (A12) can be expressed as

$$\det(\mathbb{J} - \beta \mathbb{I}) = p(\beta) = \beta^4 + \omega_x^2 \beta^2 - 2\omega_x^2 \omega_y^2. \quad (\text{A13})$$

Let $\alpha = \beta^2$; then the roots of the above polynomial are $\sqrt{\alpha_1}, -\sqrt{\alpha_1}, \sqrt{\alpha_2}, -\sqrt{\alpha_2}$, where

$$\begin{aligned} \alpha_1 &= \frac{-\omega_x^2 + \sqrt{\omega_x^2 + 8\omega_x^2 \omega_y^2}}{2}, \\ \alpha_2 &= \frac{-\omega_x^2 - \sqrt{\omega_x^2 + 8\omega_x^2 \omega_y^2}}{2}. \end{aligned} \quad (\text{A14})$$

It is clear that $\alpha_1 > 0$ and $\alpha_2 < 0$, so let us define $\lambda = \sqrt{\alpha_1}$ and $\omega = \sqrt{-\alpha_2}$, so the eigenvalues are $\lambda, -\lambda, i\omega, -i\omega$. This implies the equilibrium point is of type saddle \times center type, or *index-1 saddle*.

As shown above, the eigenvalues are of the form $\lambda, -\lambda, i\omega, -i\omega$, where

$$\lambda^2 = \alpha_1 = \frac{-\omega_x^2 + \sqrt{\omega_x^2 + 8\omega_x^2\omega_y^2}}{2},$$

$$\omega^2 = -\alpha_2 = \frac{\omega_x^2 + \sqrt{\omega_x^2 + 8\omega_x^2\omega_y^2}}{2} \quad (\text{A15})$$

and the eigenvectors as obtained in Appendix A 1 b are

$$u_\lambda = \left[1, -\frac{\lambda^2 + \omega_x^2}{\sqrt{2\omega_x\omega_y}}, \lambda, -\frac{\lambda(\lambda^2 + \omega_x^2)}{\sqrt{2\omega_x\omega_y}} \right],$$

$$u_{-\lambda} = \left[1, -\frac{\lambda^2 + \omega_x^2}{\sqrt{2\omega_x\omega_y}}, -\lambda, \frac{\lambda(\lambda^2 + \omega_x^2)}{\sqrt{2\omega_x\omega_y}} \right] \quad (\text{A16})$$

and

$$w_{i\omega} = \left[1, \frac{\omega^2 - \omega_x^2}{\sqrt{2\omega_x\omega_y}}, i\omega, \frac{i\omega(\omega^2 - \omega_x^2)}{\sqrt{2\omega_x\omega_y}} \right],$$

$$w_{-i\omega} = \left[1, \frac{\omega^2 - \omega_x^2}{\sqrt{2\omega_x\omega_y}}, -i\omega, -\frac{i\omega(\omega^2 - \omega_x^2)}{\sqrt{2\omega_x\omega_y}} \right]. \quad (\text{A17})$$

b. Eigenvectors of linearized system

Let us assume the eigenvector to be $v = [k_1, k_2, k_3, k_4]^T$, and the eigenvalue problem becomes $\mathbb{J}v = \beta v$. This gives the expressions

$$k_3 = \beta k_1, \quad (\text{A18})$$

$$k_4 = \beta k_2, \quad (\text{A19})$$

$$-\omega_x^2 k_1 - \sqrt{2}\omega_x\omega_y k_2 = \beta k_3, \quad (\text{A20})$$

$$-\sqrt{2}\omega_x\omega_y k_1 = \beta k_4. \quad (\text{A21})$$

Let $k_1 = 1$; then using Eqs. (A18) and (A19) the eigenvector becomes $[1, k_2, \beta, \beta k_2]^T$.

Then, using Eqs. (A20) and (A21) for eigenvalue $\beta = \pm\lambda$, we get

$$-\omega_x^2 - \sqrt{2}\omega_x\omega_y k_2 = \lambda^2,$$

$$-\sqrt{2}\omega_x\omega_y = \lambda k_2,$$

$$-\omega_x^2 - \sqrt{2}\omega_x\omega_y k_2' = \lambda^2,$$

$$-\sqrt{2}\omega_x\omega_y = \lambda k_2'. \quad (\text{A22})$$

These imply $k_2 = k_2'$ and

$$k_2 = -\frac{\lambda^2 + \omega_x^2}{\sqrt{2}\omega_x\omega_y}. \quad (\text{A23})$$

A similar approach for the eigenvalues, $\beta = \pm i\omega$, gives us

$$k_2 = \frac{\omega^2 - \omega_x^2}{\sqrt{2}\omega_x\omega_y}. \quad (\text{A24})$$

Thus the eigenvectors corresponding to $\pm\lambda$ are

$$u_\lambda = \left[1, -\frac{\lambda^2 + \omega_x^2}{\sqrt{2}\omega_x\omega_y}, \lambda, -\frac{\lambda(\lambda^2 + \omega_x^2)}{\sqrt{2}\omega_x\omega_y} \right],$$

$$u_{-\lambda} = \left[1, -\frac{\lambda^2 + \omega_x^2}{\sqrt{2}\omega_x\omega_y}, -\lambda, \frac{\lambda(\lambda^2 + \omega_x^2)}{\sqrt{2}\omega_x\omega_y} \right], \quad (\text{A25})$$

and for the eigenvalues, $\pm i\omega$, we obtain

$$w_{i\omega} = \left[1, \frac{\omega^2 - \omega_x^2}{\sqrt{2}\omega_x\omega_y}, i\omega, \frac{i\omega(\omega^2 - \omega_x^2)}{\sqrt{2}\omega_x\omega_y} \right],$$

$$w_{-i\omega} = \left[1, \frac{\omega^2 - \omega_x^2}{\sqrt{2}\omega_x\omega_y}, -i\omega, -\frac{i\omega(\omega^2 - \omega_x^2)}{\sqrt{2}\omega_x\omega_y} \right], \quad (\text{A26})$$

where λ and ω are positive constants (A14) that depend on the parameters of the potential energy surface. Thus the general solution of the linear system near the saddle equilibrium point is given by

$$\mathbf{x}(t) = \{x(t), y(t), v_x(t), v_y(t)\}$$

$$= A_1 e^{\lambda t} u_\lambda + A_2 e^{-\lambda t} u_{-\lambda} + 2 \operatorname{Re}(\beta e^{i\omega t} w_{i\omega}), \quad (\text{A27})$$

with A_1, A_2 being real and $\beta = \beta_1 + i\beta_2$ being complex.

2. Computing the NHIM and its invariant manifolds associated with the index-1 saddle

For discussing the geometry, we call the equilibrium with positive y -coordinate $\mathbf{x}_{\text{eq,top}}$ and negative y -coordinate $\mathbf{x}_{\text{eq,bot}}$.

Select appropriate energy above the critical value. For computation of manifolds that act as boundary between the transition and nontransition trajectories, we select the total energy, E , above the critical value and so the excess energy $\Delta E > 0$. This excess energy can be arbitrarily large as long as the energy surface stays within the dynamical system's phase space bounds.

Differential correction and numerical continuation for the NHIM. We consider a procedure which computes periodic orbits around in a relatively straightforward fashion. This procedure begins with small “seed” initial conditions obtained from the linearized equations of motion near $\mathbf{x}_{\text{eq,bot}}$ [87] and uses differential correction and numerical continuation to generate the desired periodic orbit corresponding to the chosen energy E [88]. The result is a periodic orbit of the desired energy E of some period T , which will be close to $2\pi/\omega$ where $\pm i\omega$ is the imaginary pair of eigenvalues of the linearization around the saddle point.

Guess initial condition of the periodic orbit. The linearized equations of motion near an equilibrium point can be used to initialize a guess for the differential correction method. Let us select the equilibrium point, $\mathbf{x}_{\text{eq,bot}}$. The linearization yields an eigenvalue problem $Av = \gamma v$, where A is the Jacobian matrix (A10) evaluated at the equilibrium point, γ is the eigenvalue, and $v = [k_1, k_2, k_3, k_4]^T$ is the corresponding eigenvector. Thus, using the structure of A from Eq. (A10), we can write

$$k_3 = \gamma k_1,$$

$$k_4 = \gamma k_2, \quad (\text{A28})$$

$$ak_1 + bk_2 = \gamma k_3,$$

$$ck_1 + dk_2 = \gamma k_4,$$

where a, b, c, d are entries in the Jacobian (A10) and evaluated at the equilibrium point $(x_{\text{eq,bot}}, y_{\text{eq,bot}}, 0, 0)$. So when $\gamma = \pm\lambda$, which corresponds to the saddle directions of the equilibrium point, the corresponding eigenvectors are

$$u_1 = [1, k_2, \lambda, \lambda k_2],$$

$$u_2 = [1, k_2, -\lambda, -\lambda k_2], \quad (\text{A29})$$

and when $\gamma = \pm i\omega$, which corresponds to the center directions, the corresponding eigenvectors are

$$\begin{aligned} w_1 &= [1, k_2, i\omega, i\omega k_2], \\ w_2 &= [1, k_2, -i\omega, -i\omega k_2], \end{aligned} \quad (\text{A30})$$

where $k_2 = (\gamma^2 - a)/b$ is the constant depending on the eigenvalue, γ . Thus the general solution of the linearized equation of motion in Eq. (A27) can be used to initialize a guess for the periodic orbit for a small amplitude, $A_x \approx 10^{-4}$. The idea is to use the complex eigenvalue and the corresponding eigenvector to obtain a starting guess for the initial condition on the periodic orbit and its period T_{po} , which should be close to $2\pi/\omega$ (generalization of Liapounov's theorem) and increase monotonically with excess energy, ΔE .

The initial condition for a periodic orbit of x amplitude, $A_x > 0$, can be computed by letting $A_1 = A_2 = 0$ and $t = 0$ in Eq. (A27), and $\beta = -A_x/2$ (this choice is made to get rid of factor 2) denotes a small amplitude in the general linear solution. Thus, using the eigenvector along the center direction, we can guess the initial condition to be

$$\begin{aligned} \bar{\mathbf{x}}_{0,g} &= (x_{\text{eq,bot}}, y_{\text{eq,bot}}, 0, 0)^T + 2 \text{Re}(\beta w_1) \\ &= (x_{\text{eq,bot}} - A_x, y_{\text{eq,bot}} - A_x k_2, 0, 0)^T. \end{aligned} \quad (\text{A31})$$

Without loss of generality, let us consider the bottom index-1 saddle equilibrium point (on the potential energy surface, $y < 0$); then the initial guess is given by

$$\bar{\mathbf{x}}_{0,g} = \left(-\frac{\omega_y^2}{2\delta} - A_x, -\frac{1}{\sqrt{2}} \frac{\omega_x \omega_y}{\delta} - \frac{A_x(\omega^2 - \omega_x^2)}{\sqrt{2}\omega_x \omega_y}, 0, 0 \right). \quad (\text{A32})$$

Differential correction of the initial condition. In this procedure, we attempt to introduce small change in the initial guess such that the periodic orbit $\bar{\mathbf{x}}_{\text{po}}$

$$\|\bar{\mathbf{x}}_{\text{po}}(T) - \bar{\mathbf{x}}_{\text{po}}(0)\| < \epsilon \quad (\text{A33})$$

for some tolerance $\epsilon \ll 1$. In this approach, we hold x coordinate constant, while applying correction to the initial guess of the y coordinate, use v_y coordinate for terminating event-based integration, and v_x coordinate to test convergence of the periodic orbit. It is to be noted that this combination of coordinates is suitable for the structure of the initial guess at hand, and in general will require some permutation of the phase space coordinates to achieve a stable algorithm.

Let us denote the flow map of a differential equation $\dot{\mathbf{x}} = \mathbf{f}(\mathbf{x})$ with initial condition $\mathbf{x}(t_0) = \mathbf{x}_0$ by $\phi(t; \mathbf{x}_0)$. Thus the displacement of the final state under a perturbation δt becomes

$$\delta \bar{\mathbf{x}}(t + \delta t) = \phi(t + \delta t; \bar{\mathbf{x}}_0 + \delta \bar{\mathbf{x}}_0) - \phi(t; \bar{\mathbf{x}}_0), \quad (\text{A34})$$

with respect to the reference orbit $\bar{\mathbf{x}}(t)$. Thus measuring the displacement at $t_1 + \delta t_1$ and expanding into Taylor series gives

$$\delta \bar{\mathbf{x}}(t_1 + \delta t_1) = \frac{\partial \phi(t_1; \bar{\mathbf{x}}_0)}{\partial \mathbf{x}_0} \delta \bar{\mathbf{x}}_0 + \frac{\partial \phi(t_1; \bar{\mathbf{x}}_0)}{\partial t_1} \delta t_1 + h.o.t., \quad (\text{A35})$$

where the first term on the right hand side is the state transition matrix, $\Phi(t_1, t_0)$, when $\delta t_1 = 0$. Thus it can be obtained as the numerical solution to the variational equations as discussed in

[89]. Let us suppose we want to reach the desired point \mathbf{x}_d ; we have

$$\bar{\mathbf{x}}(t_1) = \phi(t_1; \bar{\mathbf{x}}_0) = \bar{\mathbf{x}}_1 = \mathbf{x}_d - \delta \bar{\mathbf{x}}_1, \quad (\text{A36})$$

which has an error $\delta \bar{\mathbf{x}}_1$ and needs correction. This correction to the first order can be obtained from the state transition matrix at t_1 and an iterative procedure of this small correction based on first order yields convergence in a few steps. For the equilibrium point under consideration, we initialize the guess as

$$\bar{\mathbf{x}}(0) = (x_{0,g}, y_{0,g}, 0, 0)^T \quad (\text{A37})$$

and using the numerical integrator we continue until the next $v_x = 0$ event crossing with a high specified tolerance (typically 10^{-14}). So, we obtain $\bar{\mathbf{x}}(t_1)$ which for the guess periodic orbit denotes the half-period point, $t_1 = T_{0,g}/2$, and compute the state transition matrix $\Phi(t_1, 0)$. This can be used to correct the initial value of $y_{0,g}$ to approximate the periodic orbit while keeping $x_{0,g}$ constant. Thus correction to the first order is given by

$$\delta v_{x_1} = \Phi_{32} \delta y_0 + \dot{v}_{x_1} \delta t_1 + h.o.t., \quad (\text{A38})$$

$$\delta v_{y_1} = \Phi_{42} \delta y_0 + \dot{v}_{y_1} \delta t_1 + h.o.t., \quad (\text{A39})$$

where Φ_{ij} is the (i, j) th entry of $\Phi(t_1, 0)$ and the acceleration terms come from the equations of motion evaluated at the crossing $t = t_1$ when $v_{x_1} = \delta v_{x_1} = 0$. Thus we obtain the first order correction δy_0 as

$$\delta y_0 \approx \left(\Phi_{42} - \Phi_{32} \frac{\dot{v}_{y_1}}{\dot{v}_{x_1}} \right)^{-1} \delta v_{y_1}, \quad (\text{A40})$$

$$y_0 \rightarrow y_0 - \delta y_0, \quad (\text{A41})$$

which is iterated until $|v_{y_1}| = |\delta v_{y_1}| < \epsilon$ for some tolerance ϵ , since we want the final periodic orbit to be of the form

$$\bar{\mathbf{x}}_{t_1} = (x_1, y_1, 0, 0)^T. \quad (\text{A42})$$

This procedure yields an accurate initial condition for a periodic orbit of small amplitude $A_x \ll 1$, since our initial guess is based on the linear approximation near the equilibrium point. It is also to be noted that differential correction assumes the guess periodic orbit has a small error (for example, in this system, of the order of 10^{-2}) and can be corrected using first order form of the correction terms. If, however, larger steps in correction are applied this can lead to unstable convergence as the half-orbit overshoots between successive steps. Even though there are other algorithms for detecting unstable periodic orbits, differential correction is easy to implement and shows reliable convergence for generating a family of periodic orbits at arbitrary high excess energy near the index-1 saddle.

Numerical continuation to periodic orbit at arbitrary energy. The procedure described above yields an accurate initial condition for a periodic orbit from a single initial guess. If our initial guess came from the linear approximation near the equilibrium point, from Eq. (A27), it has been observed numerically that we can only use this procedure for small amplitude, of order 10^{-4} , periodic orbits around $\mathbf{x}_{\text{eq,bot}}$. This small amplitude corresponds to small excess energy, typically of the order 10^{-2} , and if we want to compute the periodic orbit

of arbitrarily large amplitude, we resort to numerical continuation for generating a family which reaches the appropriate total energy. This is done using two nearby periodic orbits of small amplitude to obtain an initial guess for the next periodic orbit and performing differential correction to this guess. To this end, we proceed as follows. Suppose we find two small nearby periodic orbit initial conditions, $\bar{x}_0^{(1)}$ and $\bar{x}_0^{(2)}$, correct to within the tolerance d_{tol} , using the differential correction procedure described above. We can generate a family of periodic orbits with successively increasing amplitudes around $\bar{x}_{\text{eq,bot}}$ in the following way. Let

$$\Delta = \bar{x}_0^{(2)} - \bar{x}_0^{(1)} = [\Delta x_0, \Delta y_0, 0, 0]^T. \quad (\text{A43})$$

A linear extrapolation to an initial guess of slightly larger amplitude, $\bar{x}_0^{(3)}$, is given by

$$\begin{aligned} \bar{x}_{0,g}^{(3)} &= \bar{x}_0^{(2)} + \Delta \\ &= [(\bar{x}_0^{(2)} + \Delta x_0), (y_0^{(2)} + \Delta y_0), 0, 0]^T \\ &= [x_0^{(3)}, y_0^{(3)}, 0, 0]^T. \end{aligned} \quad (\text{A44})$$

Thus, keeping $x_0^{(3)}$ fixed, we can use differential correction on this initial condition to compute an accurate solution $\bar{x}_0^{(3)}$ from the initial guess $\bar{x}_{0,g}^{(3)}$ and repeat the process until we have a family of solutions. We can keep track of the energy of each periodic orbit and when we have two solutions, $\bar{x}_0^{(k)}$ and $\bar{x}_0^{(k+1)}$, whose energy brackets the appropriate energy, E , we can resort to combining bisection and differential correction to these two periodic orbits until we converge to the desired periodic orbit to within a specified tolerance. Thus the result is a periodic orbit at desired total energy E and of some period T with an initial condition X_0 . This is shown in Fig. 6 for a series of excess energy at intervals of 0.250.

Globalization of invariant manifolds. We find the local approximation to the unstable and stable manifolds of the periodic orbit from the eigenvectors of the monodromy matrix. Next, the local linear approximation of the unstable (or stable) manifold in the form of a state vector is integrated in the nonlinear equations of motion to produce the approximation of the unstable (or stable) manifolds. This procedure is known as *globalization of the manifolds* and we proceed as follows.

First, the state transition matrix $\Phi(t)$ along the periodic orbit with initial condition X_0 can be obtained numerically by integrating the variational equations along with the equations of motion from $t = 0$ to $t = T$. This is known as the monodromy matrix $M = \Phi(T)$ and the eigenvalues can be computed numerically. For Hamiltonian systems (see [90] for details), this tells us that the four eigenvalues of M are of the form

$$\lambda_1 > 1, \quad \lambda_2 = \frac{1}{\lambda_1}, \quad \lambda_3 = \lambda_4 = 1. \quad (\text{A45})$$

The eigenvector associated with eigenvalue λ_1 is in the unstable direction; the eigenvector associated with eigenvalue λ_2 is in the stable direction. Let $e^s(X_0)$ denote the normalized (to 1) stable eigenvector and $e^u(X_0)$ denote the normalized unstable eigenvector. We can compute the manifold by initializing along these eigenvectors as

$$X^s(X_0) = X_0 + \epsilon e^s(X_0) \quad (\text{A46})$$

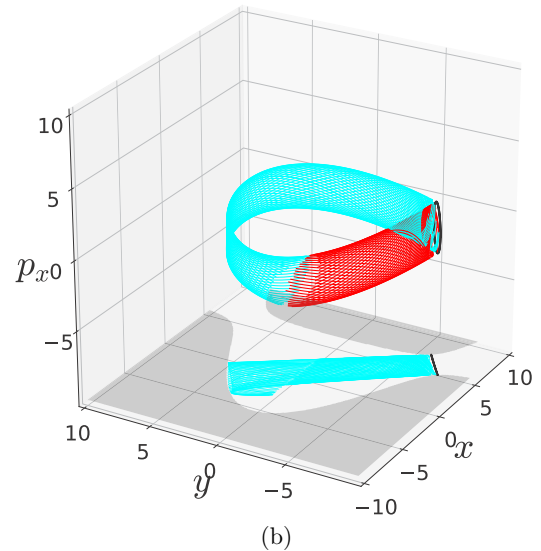
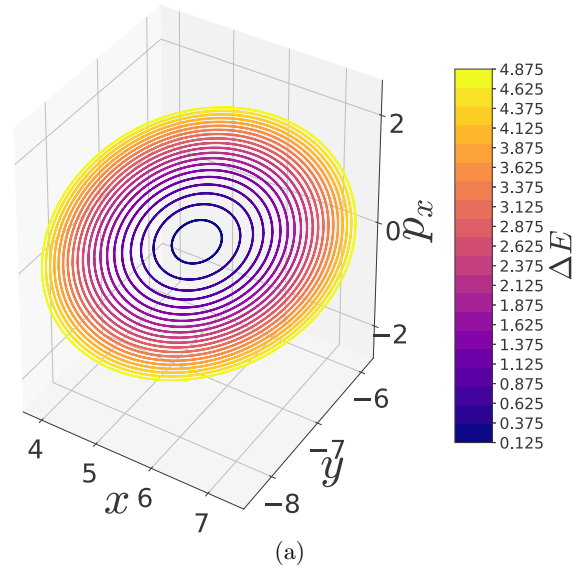


FIG. 6. Unstable periodic orbits at interval of $\Delta E = 0.25$ starting from $\Delta E = 0.125$ around the bottom saddle equilibrium point. The stable and unstable manifolds associated with the unstable periodic orbit (NHIM of dimension 1) around the same equilibrium point at $\Delta E = 2.25$.

for the stable manifold at X_0 along the periodic orbit as

$$X^u(X_0) = X_0 + \epsilon e^u(X_0) \quad (\text{A47})$$

for the unstable manifold at X_0 . Here the small displacement from X_0 is denoted by ϵ and its magnitude should be small enough to be within the validity of the linear estimate, yet not so small that the time of flight becomes too large due to the asymptotic nature of the stable and unstable manifolds. Reference [88] suggests typical values of $\epsilon > 0$ corresponding to nondimensional position displacements of magnitude around 10^{-6} . By numerically integrating the unstable vector forward in time, using both ϵ and $-\epsilon$, for the forward and backward branches, respectively, we generate trajectories shadowing the two branches, W_+^u and W_-^u , of the unstable manifold of the periodic orbit. Similarly, by integrating the stable vector

backwards in time, using both ϵ and $-\epsilon$, for forward and backward branches, respectively, we generate trajectories shadowing the stable manifold, $W_{+,-}^s$. For the manifold at $X(t)$, one can simply use the state transition matrix to transport the eigenvectors from X_0 to $X(t)$ as

$$X^s(X(t)) = \Phi(t, 0)X^s(X_0). \quad (\text{A48})$$

It is to be noted that, since the state transition matrix does not preserve the norm, the resulting vector must be normalized. The globalized invariant manifolds associated with index-1 saddles are known as Conley-McGehee tubes [91]. These tubes form the skeleton of transition dynamics by acting as conduits for the states inside them to travel between potential wells.

The computation of codimension-1 separatrix associated with the unstable periodic orbit around an index-1 saddle begins with the linearized equations of motion. This is obtained after a coordinate transformation to the saddle equilibrium point and Taylor expansion of the equations of motion. Keeping the first order terms in this expansion, we obtain the eigenvalues and eigenvectors of the linearized system. The eigenvectors corresponding to the center direction provide the starting guess for computing the unstable periodic orbits for small excess energy, $\Delta E \ll 1$, above the saddle's energy. This iterative procedure performs a small correction to the starting guess based on the terminal condition of the periodic orbit until a desired tolerance is satisfied. This procedure is known as differential correction and generates unstable periodic orbits for small excess energy. Next, a numerical continuation is implemented to follow the small energy (amplitude) periodic orbits out to high excess energies. We apply this procedure to the Barbanis two DOF system in Sec. II A to generate the unstable periodic orbit and its associated invariant manifolds as shown in Fig. 6.

APPENDIX B: COUPLED HARMONIC THREE DOF SYSTEM

For the system (4), Hamilton's equations of motion are

$$\dot{x} = \frac{\partial V_{\text{BC}}}{\partial p_x} = p_x,$$

$$\dot{y} = \frac{\partial V_{\text{BC}}}{\partial p_y} = p_y,$$

$$\dot{\mathbf{x}} = \mathbb{J}|_{\mathbf{x}_{\text{eq}}} \mathbf{x} = Df(\mathbf{x})|_{\mathbf{x}_{\text{eq}}} \mathbf{x}$$

$$\dot{\mathbf{x}} = \begin{pmatrix} 0 & 0 & 0 & 1 & 0 & 0 \\ 0 & 0 & 0 & 0 & 1 & 0 \\ 0 & 0 & 0 & 0 & 0 & 1 \\ -(\omega_x^2 - 2\epsilon y_e - 2\eta z_e) & 2\epsilon x_e & 2\eta x_e & 0 & 0 & 0 \\ 2\epsilon x_e & -\omega_y^2 & 0 & 0 & 0 & 0 \\ -2\eta x_e & 0 & -\omega_z^2 & 0 & 0 & 0 \end{pmatrix} \begin{bmatrix} x \\ y \\ z \\ p_x \\ p_y \\ p_z \end{bmatrix}. \quad (\text{B5})$$

$$\dot{z} = \frac{\partial V_{\text{BC}}}{\partial p_z} = p_z,$$

$$\dot{p}_x = -\frac{\partial V_{\text{BC}}}{\partial x} = -(\omega_x^2 x - 2\epsilon xy - 2\eta xz),$$

$$\dot{p}_y = -\frac{\partial V_{\text{BC}}}{\partial y} = -(\omega_y^2 y - \epsilon x^2),$$

$$\dot{p}_z = -\frac{\partial V_{\text{BC}}}{\partial z} = -(\omega_z^2 z - \eta x^2). \quad (\text{B1})$$

Symmetries of the equations of motion. We note the symmetries in the system (B1), by substituting $(-x, -p_x)$ for (x, p_x) , which implies reflection about the $x = 0$ plane and is expressed as

$$s_x : (x, y, z, p_x, p_y, p_z, t) \rightarrow (-x, y, z, -p_x, p_y, p_z, t). \quad (\text{B2})$$

Thus, if $[x(t), y(t), z(t), p_x(t), p_y(t), p_z(t)]$ is a solution to (B1), then $[-x(t), y(t), z(t), -p_x(t), p_y(t), p_z(t)]$ is another solution. The conservative system also has time-reversal symmetry

$$s_t : (x, y, z, p_x, p_y, p_z, t) \rightarrow (x, y, z, -p_x, -p_y, -p_z, t). \quad (\text{B3})$$

Combining the two symmetries, if $[x(t), y(t), z(t), p_x(t), p_y(t), p_z(t)]$ is a solution to (B1), then $[x(-t), y(-t), z(-t), -p_x(-t), -p_y(-t), -p_z(-t)]$ is another solution. These symmetries will be used to decrease the number of computations and to find special solutions. For example, any solution of (B1) will evolve on the energy surface given by (4). For a fixed energy, $E(x, y, z, p_x, p_y, p_z) = e$, there is a zero velocity surface corresponding to $V_{\text{BC}}(x, y, z) = e$, the contours shown in Fig. 1(a). Any trajectory which touches the zero velocity curve at time t_0 must retrace its path in configuration space [i.e., $q = (x, y, z)$ space],

$$q(-t + t_0) = q(t + t_0), \quad \dot{q}(-t + t_0) = -\dot{q}(t + t_0). \quad (\text{B4})$$

Linear system near equilibrium point. Here we study the dynamics near the equilibrium points using linearization of the vector field (B1) given by the Jacobian, $Df(\mathbf{x})$ of the vector field evaluated at the equilibrium point, $\mathbf{x}_{\text{eq}} = (x_e, y_e, z_e, 0, 0, 0)$:

[1] T. Komatsuzaki and R. S. Berry, *J. Chem. Phys.* **110**, 9160 (1999).

[2] S. Wiggins, L. Wiesenfeld, C. Jaffé, and T. Uzer, *Phys. Rev. Lett.* **86**, 5478 (2001).

- [3] T. Komatsuzaki and R. S. Berry, *Proc. Natl. Acad. Sci. USA* **98**, 7666 (2001).
- [4] C. Jaffé, D. Farrelly, and T. Uzer, *Phys. Rev. Lett.* **84**, 610 (2000).
- [5] B. Eckhardt, *J. Phys. A* **28**, 3469 (1995).
- [6] P. Collins, G. S. Ezra, and S. Wiggins, *Phys. Rev. E* **86**, 056218 (2012).
- [7] J. Zhong, L. N. Virgin, and S. D. Ross, *Int. J. Mech. Sci.* **149**, 413 (2018).
- [8] L. N. Virgin, *Dyn. Stability Syst.* **4**, 56 (1989).
- [9] J. M. T. Thompson and J. R. de Souza, *Proc. R. Soc. London A* **452**, 2527 (1996).
- [10] S. Naik and S. D. Ross, *Commun. Nonlinear Sci.* **47**, 48 (2017).
- [11] C. Jaffé, S. D. Ross, M. W. Lo, J. E. Marsden, D. Farrelly, and T. Uzer, *Phys. Rev. Lett.* **89**, 011101 (2002).
- [12] M. Dellnitz, O. Junge, M. W. Lo, J. E. Marsden, K. Padberg, R. Preis, S. D. Ross, and B. Thiere, *Phys. Rev. Lett.* **94**, 231102 (2005).
- [13] S. D. Ross, in *Libration Point Orbits and Applications*, edited by G. Gómez, M. W. Lo, and J. J. Masdemont (World Scientific, Singapore, 2003), pp. 637–652.
- [14] H. P. de Oliveira, A. M. Ozorio de Almeida, I. Damião Soares, and E. V. Tonini, *Phys. Rev. D* **65**, 083511 (2002).
- [15] R. S. MacKay, *Phys. Lett. A* **145**, 425 (1990).
- [16] R. S. MacKay, J. D. Meiss, and I. C. Percival, *Physica D (Amsterdam, Neth.)* **13**, 55 (1984).
- [17] S. D. Ross, A. E. BozorgMagham, S. Naik, and L. N. Virgin, *Phys. Rev. E* **98**, 052214 (2018).
- [18] S. Patra and S. Keshavamurthy, *Chem. Phys. Lett.* **634**, 1 (2015).
- [19] A. Junginger, L. Duvenbeck, M. Feldmaier, J. Main, G. Wunner, and R. Hernandez, *J. Chem. Phys.* **147**, 064101 (2017).
- [20] A. Junginger, G. T. Craven, T. Bartsch, F. Revuelta, F. Borondo, R. Benito, and R. Hernandez, *Phys. Chem. Chem. Phys.* **18**, 30270 (2016).
- [21] S. Patra and S. Keshavamurthy, *Phys. Chem. Chem. Phys.* **20**, 4970 (2018).
- [22] S. Naik, V. J. García-Garrido, and S. Wiggins, *Commun. Nonlinear Sci. Numer.* **79**, 104907 (2019).
- [23] B. Barbanis, *Astron. J.* **71**, 415 (1966).
- [24] P. Brumer and J. W. Duff, *J. Chem. Phys.* **65**, 3566 (1976).
- [25] M. J. Davis and E. J. Heller, *J. Chem. Phys.* **71**, 3383 (1979).
- [26] E. J. Heller, E. B. Stechel, and M. J. Davis, *J. Chem. Phys.* **73**, 4720 (1980).
- [27] B. A. Waite and W. H. Miller, *J. Chem. Phys.* **74**, 3910 (1981).
- [28] R. Kosloff and S. A. Rice, *J. Chem. Phys.* **74**, 1947 (1981).
- [29] G. Contopoulos and P. Magnenat, *Celest. Mech.* **37**, 387 (1985).
- [30] M. Founargiotakis, S. C. Farantos, G. Contopoulos, and C. Polymilis, *J. Chem. Phys.* **91**, 1389 (1989).
- [31] B. Barbanis, *Celest. Mech. Dyn. Astron.* **48**, 57 (1990).
- [32] D. Babyuk, R. E. Wyatt, and J. H. Frederick, *J. Chem. Phys.* **119**, 6482 (2003).
- [33] G. Contopoulos, *Astron. J.* **75**, 96 (1970).
- [34] G. Contopoulos, S. C. Farantos, H. Papadaki, and C. Polymilis, *Phys. Rev. E* **50**, 4399 (1994).
- [35] J. Aguirre, J. C. Vallejo, and M. A. F. Sanjuán, *Phys. Rev. E* **64**, 066208 (2001).
- [36] M. Hénon and C. Heiles, *Astron. J.* **69**, 73 (1964).
- [37] M. Hénon, *Phys. Rev. B* **9**, 1921 (1974).
- [38] M. Toda, *Phys. Lett. A* **48**, 335 (1974).
- [39] B. Barbanis, *Celest. Mech.* **14**, 201 (1976).
- [40] D. W. Noid, M. L. Koszykowski, and R. A. Marcus, *J. Chem. Phys.* **67**, 404 (1977).
- [41] I. Hamilton and P. Brumer, *Phys. Rev. A* **23**, 1941 (1981).
- [42] R. A. Pullen and A. R. Edmonds, *J. Phys. A* **14**, L319 (1981).
- [43] Y. Y. Bai, G. Hose, C. W. McCurdy, and H. S. Taylor, *Chem. Phys. Lett.* **99**, 342 (1983).
- [44] V. L. Berdichevsky and M. V. Alberti, *Phys. Rev. A* **44**, 858 (1991).
- [45] R. Barrio, *Chaos Solitons Fractals* **25**, 711 (2005).
- [46] H. J. Zhao and M. L. Du, *Phys. Rev. E* **76**, 027201 (2007).
- [47] R. Barrio, F. Blesa, and S. Serrano, *New J. Phys.* **11**, 053004 (2009).
- [48] R. Barrio and F. Blesa, *Chaos Solitons Fractals* **41**, 560 (2009).
- [49] S. Wiggins, *Physica D (Amsterdam, Neth.)* **44**, 471 (1990).
- [50] K. A. Mitchell, J. P. Handley, B. Tighe, J. B. Delos, and S. K. Knudson, *Chaos* **13**, 880 (2003).
- [51] K. A. Mitchell, J. P. Handley, J. B. Delos, and S. K. Knudson, *Chaos* **13**, 892 (2003).
- [52] K. A. Mitchell, J. P. Handley, B. Tighe, A. Flower, and J. B. Delos, *Phys. Rev. Lett.* **92**, 073001 (2004).
- [53] N. De Leon and B. J. Berne, *J. Chem. Phys.* **75**, 3495 (1981).
- [54] K. A. Mitchell, J. P. Handley, B. Tighe, A. Flower, and J. B. Delos, *Phys. Rev. A* **70**, 043407 (2004).
- [55] K. A. Mitchell and B. Ilan, *Phys. Rev. A* **80**, 043406 (2009).
- [56] K. A. Mitchell and J. B. Delos, *Physica D (Amsterdam, Neth.)* **229**, 9 (2007).
- [57] L. Wang, H. F. Yang, X. J. Liu, H. P. Liu, M. S. Zhan, and J. B. Delos, *Phys. Rev. A* **82**, 022514 (2010).
- [58] J. A. J. Madrid and A. M. Mancho, *Chaos* **19**, 013111 (2009).
- [59] C. Mendoza and A. M. Mancho, *Phys. Rev. Lett.* **105**, 038501 (2010).
- [60] A. M. Mancho, S. Wiggins, J. Curbelo, and C. Mendoza, *Commun. Nonlinear Sci. Numer.* **18**, 3530 (2013).
- [61] C. Lopesino, F. Balibrea-Iniesta, V. J. García-Garrido, S. Wiggins, and A. M. Mancho, *Int. J. Bifurcat. Chaos* **27**, 1730001 (2017).
- [62] F. Balibrea-Iniesta, C. Lopesino, S. Wiggins, and A. M. Mancho, *Int. J. Bifurcat. Chaos* **26**, 1630036 (2016).
- [63] G. T. Craven, A. Junginger, and R. Hernandez, *Phys. Rev. E* **96**, 022222 (2017).
- [64] A. Junginger and R. Hernandez, *Phys. Chem. Chem. Phys.* **18**, 30282 (2016).
- [65] A. de la Cámara, A. M. Mancho, K. Ide, E. Serrano, and C. Mechoso, *J. Atmos. Sci.* **69**, 753 (2012).
- [66] C. Mendoza, A. M. Mancho, and S. Wiggins, *Nonlinear Process. Geophys.* **21**, 677 (2014).
- [67] V. J. García-Garrido, A. M. Mancho, and S. Wiggins, *Nonlinear Process. Geophys.* **22**, 701 (2015).
- [68] A. G. Ramos, V. J. García-Garrido, A. M. Mancho, S. Wiggins, J. Coca, S. Glenn, O. Schofield, J. Kohut, D. Aragon, J. Kerfoot, T. Haskins, T. Miles, C. Haldeman, N. Strandkov, B. Allsup, C. Jones, and J. Shapiro, *Sci. Rep.* **8**, 4575 (2018).
- [69] R. Bardakcioglu, A. Junginger, M. Feldmaier, J. Main, and R. Hernandez, *Phys. Rev. E* **98**, 032204 (2018).
- [70] G. S. Ezra and S. Wiggins, *J. Phys. Chem. A* **122**, 8354 (2018).
- [71] M. J. Davis and E. J. Heller, *J. Chem. Phys.* **75**, 246 (1981).
- [72] C. C. Martens and G. S. Ezra, *J. Chem. Phys.* **86**, 279 (1987).
- [73] S. Wiggins, *Reg. Chaotic Dyn.* **21**, 621 (2016).
- [74] S. C. Farantos, *Comput. Phys. Commun.* **108**, 240 (1998).

- [75] A. S. Demian and S. Wiggins, *Int. J. Bifurcat. Chaos* **27**, 1750225 (2017).
- [76] A. Junginger and R. Hernandez, *J. Phys. Chem. B* **120**, 1720 (2016).
- [77] A. Junginger, J. Main, G. Wunner, and R. Hernandez, *Phys. Rev. A* **95**, 032130 (2017).
- [78] C. Lopesino, F. Balibrea, S. Wiggins, and A. M. Mancho, *Commun. Nonlinear Sci. Numer. Simul.* **27**, 40 (2015).
- [79] G. T. Craven and R. Hernandez, *Phys. Chem. Chem. Phys.* **18**, 4008 (2016).
- [80] G. T. Craven and R. Hernandez, *Phys. Rev. Lett.* **115**, 148301 (2015).
- [81] M. Feldmaier, P. Schraft, R. Bardakcioglu, J. Reiff, M. Lober, M. Tschöpe, A. Junginger, J. Main, T. Bartsch, and R. Hernandez, *J. Phys. Chem. B* **123**, 2070 (2019).
- [82] J. D. Meiss, *Chaos* **7**, 139 (1997).
- [83] V. J. García-Garrido, J. Curbelo, A. M. Mancho, S. Wiggins, and C. R. Mechoso, *Reg. Chaotic Dyn.* **23**, 551 (2018).
- [84] N. De Leon, *J. Chem. Phys.* **96**, 285 (1992).
- [85] N. De Leon, M. A. Mehta, and R. Q. Topper, *J. Chem. Phys.* **94**, 8310 (1991).
- [86] N. De Leon, M. A. Mehta, and R. Q. Topper, *J. Chem. Phys.* **94**, 8329 (1991).
- [87] Equation top and Eq. bot in subscript denote the equilibrium points with positive y and negative y coordinates for the parameters chosen in this study.
- [88] W. S. Koon, M. W. Lo, J. E. Marsden, and S. D. Ross, *Dynamical Systems, the Three-body Problem and Space Mission Design* (Marsden Books, Wellington, NZ, 2011), p. 327.
- [89] T. S. Parker and L. O. Chua, *Practical Numerical Algorithms for Chaotic Systems* (Springer-Verlag, New York, 1989).
- [90] K. R. Meyer, G. R. Hall, and D. Offin, *Applied Mathematical Sciences* (Springer, Berlin, 2009).
- [91] J. E. Marsden and S. D. Ross, *Bull. Am. Math. Soc.* **43**, 43 (2006).